forum acusticum 2026
8-12 September · Graz, Austria

WAVE-BASED SIMULATION OF A BENCHMARK ROOM WITH DETAILED DIFFUSER MODELING AND SURFACE SCATTERING

Jan Wouter Smits[1], Lukas Friede[2], Albert G. Prinn[3]
[1] *The University of Edinburgh, United Kingdom*
[2] *Fraunhofer IIS, Am Wolfsmantel 33, Erlangen, 91058, Germany*
[3] *International Audio Laboratories Erlangen (A joint institution of the Friedrich-Alexander-University and Fraunhofer IIS), Am Wolfsmantel 33, Erlangen, 91058, Germany*

This paper is a revised version of the authors' submitted manuscript that was peer-reviewed by at least two anonymous reviewers.

Abstract

Room acoustic simulations often require geometry simplification to manage computational complexity, potentially introducing modeling bias. In this study, we demonstrate that a finite-difference framework can accurately simulate a measured benchmark room with complex diffusing structures while avoiding explicit geometry simplification. A geometry-based surface scattering approach is introduced, in which boundary surfaces are perturbed using a three-dimensional noise function to mitigate unrealistically specular reflections at high frequencies. The method is evaluated quantitatively against a dense measurement dataset, showing good agreement and supporting its suitability for realistic room acoustic simulation of complex environments.

Keywords: *finite differences, room acoustics, scattering*

1. Introduction

Geometrical-acoustics and finite-element room simulations typically require manual level-of-detail (LOD) reduction of detailed CAD models to reduce computational complexity [1],[2]. This process requires nontrivial decisions regarding geometric and material representation and can introduce modeling bias [3],[4],[5]. Finite-difference (FD) methods differ in that room geometry is voxelized onto a regular grid, making LOD reduction an automatic consequence of discretization rather than a manual preprocessing step. The resulting errors take the form of staircased boundaries that decrease with increasing grid resolution.

Corresponding author: *jws@possumstudios.com.*

This study demonstrates practical FD simulation of a measured benchmark room [6] containing extensive centimeter-scale geometric detail, without manual LOD reduction. By avoiding manual geometric simplification, the simulation preserves scattering from architectural features that would otherwise be removed during LOD reduction. However, even unreduced CAD models generally omit small-scale surface roughness and impedance variations, leaving a residual underrepresentation of high-frequency scattering.

In contrast to previous wave-based methods that emulate the effects of missing surface variations through modified boundary conditions [7], [8], we investigate a geometry-based approach in which boundary surfaces are perturbed using a three-dimensional noise function. The simulations employ a custom GPU-accelerated implementation of the face-centered cubic (FCC) scheme of [9], extended with frequency-dependent boundary modeling and a physically motivated source model. The proposed perturbation mitigates excessive specular reflection, substantially improving high-frequency reverberation-time predictions.

The benchmark measurements are presented in Section 2, and the FCC simulation framework is described in Section 3. Boundary materials, loudspeaker modeling, and the proposed surface-scattering approach are described in Sections 4–6, respectively. Model accuracy is evaluated against measurements in Section 7, using recently proposed validation measures [10], and the conclusions of this study are given in Section 8.

2. Room and Measurement

In this paper, the Multi-Purpose Room Impulse Response Dataset [6] is used as a benchmark to validate the presented simulation framework. This dataset contains RIRs measured on a spatially dense 3-D grid inside a complex-shaped room with a volume of approximately 139 m^3.

Figure 1: Photograph of the measurement room with the measurement robot and the loudspeakers.

A view of the room is shown in Fig. 1. Near the left wall, vertical wooden slats extend from the floor to the ceiling. The slats have a cross-section of 13 cm $\times$ 6 cm and 4 cm spacing, and are arranged to form multiple recesses, which house furniture. Horizontal wooden slats cover most of the ceiling, and the right wall is a large window with a thin curtain hanging in front of it. A robot-positioned vertical array of eight omnidirectional microphones measured room impulse responses on a 15 cm Cartesian grid for eight loudspeaker positions, yielding 68,736 RIRs. The simulations in this paper were performed for speaker S4, which is a cubic-shaped custom-built speaker with an 8-inch driver. Reference microphones were positioned close to the speaker for calibration, as pictured in Fig. 2.

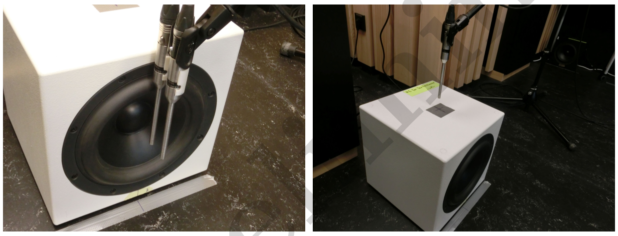

Figure 2: Close microphone positions for speaker calibration: (left) difference pair, (right) on-device microphone.

3. Simulation Technique

The governing equation considered is the lossless homogeneous acoustic wave equation in air

$$\partial_{tt} p = c_0^2 \Delta p, \tag{1}$$

where acoustic pressure p is a function of position $\boldsymbol{x} \in \Omega$ and time $t \geq 0$, and c_0 is the constant ambient wavespeed in air, set here as $c_0 = 343$ m/s. Boundary conditions on the domain boundary $\partial\Omega$ are defined in the frequency domain, as

$$-\boldsymbol{n} \cdot \nabla \hat{p} = \frac{\mathrm{i}\omega \hat{Y}}{c_0} \hat{p} + \mathrm{i}\omega \rho_0 \hat{Q}, \quad \boldsymbol{x} \in \partial\Omega, \tag{2}$$

where $\boldsymbol{n}$ is the outward-pointing normal vector of the boundary, ρ_0 is the ambient air density, set to 1.21 kg/m^3, and $\hat{Y}$ is the complex frequency-dependent normalized (dimensionless) admittance (scaled by $\rho_0 c_0$). A boundary-normal velocity source term $\hat{Q}$ has been added to model the speaker cones. The admittances are specified as passive (positive-real) rational functions

$$\hat{Y} = Y_\infty + \sum_{m=1}^{M} \frac{A^{(m)}}{\mathrm{i}\omega - \eta^{(m)}}. \tag{3}$$

Here, Y_∞ is the (real-valued) high-frequency asymptotic value, η are the poles, which must lie in the closed complex left half-plane for stability, and A are the associated residues. Via inverse Fourier transform, the boundary relation ($\boldsymbol{x} \in \partial\Omega$) is then formulated using an auxiliary differential equation approach

$$-\boldsymbol{n} \cdot \nabla p = \frac{Y_\infty}{c_0} \partial_t p + \frac{1}{c_0} \sum_{m=1}^{M} A^{(m)} \partial_t \phi^{(m)} + \rho_0 \partial_t Q, \tag{4}$$

in combination with M first-order auxiliary equations for the state variables ϕ:

$$\frac{\mathrm{d}\phi^{(m)}}{\mathrm{d}t} - \eta^{(m)} \phi^{(m)} = p, \quad m = 1 \ldots M. \tag{5}$$

Equation (1) is discretized using a 13-point face-centered cubic (FCC) finite-difference scheme, which is equivalent to finite-volume discretization with a rhombic dodecahedral cell shape [9]. The resulting difference equation is

$$p_{\boldsymbol{i}}^{n+1} - 2p_{\boldsymbol{i}}^{n} + p_{\boldsymbol{i}}^{n-1} = \frac{\lambda^2}{4} \sum_{\boldsymbol{j} \in \mathcal{R}} (p_{\boldsymbol{i}+\boldsymbol{j}}^{n} - p_{\boldsymbol{i}}^{n}), \quad \boldsymbol{i} \in \mathcal{I}, \tag{6}$$

where n is the time index for $t = nT$ with time step T, $\boldsymbol{i}$ is a position index such that $\boldsymbol{x} = \boldsymbol{i}X$ for grid step X and λ is the Courant number $\lambda := c_0 T/X$. $\mathcal{I}$ is the discrete set of indices corresponding to Ω, constrained to even-sum grid points by the FCC lattice: $\mathcal{I} = \{\boldsymbol{i} \in \mathbb{Z}^3 | \boldsymbol{i}X \in \Omega, i_1 + i_2 + i_3 \bmod 2 = 0\}$. $\mathcal{R}$ contains the twelve neighbor offsets of the FCC stencil.

To discretize (4), we apply the method proposed in [11, Eq. (20)-(21)] and add the auxiliary state and source terms to give

$$\begin{aligned} -(p_{\boldsymbol{i}+\boldsymbol{j}}^{n} - p_{\boldsymbol{i}}^{n}) = \frac{\boldsymbol{n} \cdot \boldsymbol{j}}{2\lambda} \Big(& Y_\infty (p_{\boldsymbol{i}}^{n+1} - p_{\boldsymbol{i}}^{n-1}) \\ & + \sum_{m=1}^{M} A^{(m)} (\phi_{\boldsymbol{i}}^{(m),n+1} - \phi_{\boldsymbol{i}}^{(m),n-1}) \\ & + \rho_0 c_0 (Q_{\boldsymbol{i}}^{n+1} - Q_{\boldsymbol{i}}^{n-1}) \Big), \quad \boldsymbol{j} \in \mathcal{R}, (\boldsymbol{i}+\boldsymbol{j})X \notin \Omega. \end{aligned} \tag{7}$$

Via trapezoidal (bilinear) discretization, the auxiliary state equations (5) become

$$(2-\eta^{(m)}T)\phi_{\boldsymbol{i}}^{(m),n+1}-(2+\eta^{(m)}T)\phi_{\boldsymbol{i}}^{(m),n} \\ = T(p_{\boldsymbol{i}}^{n+1}+p_{\boldsymbol{i}}^{n}). \quad (8)$$

The complete system is assembled by combining the discretized wave equation (6) with the boundary relation (7), eliminating the unknown *ghost-node* pressures $p_{\boldsymbol{i}+\boldsymbol{j}}$, $\boldsymbol{i}+\boldsymbol{j}\notin\mathcal{I}$. This results in an explicit two-step update equation which can be evaluated efficiently in a finite-difference recursion loop.
The stable limit for the Courant number for the FCC scheme can be found through von Neumann analysis as $\lambda\leq 1$. Another important consideration is the numerical dispersion error, which should ideally be kept small enough to be imperceptible. In the study in [12], this perception limit is estimated at around 2% for small, well-damped rooms. In the simulations of this paper, a spatial resolution of $X = 4$ mm was used, corresponding to a frequency range of 15.3 kHz for the aforementioned numerical dispersion error limit (see the analysis method in [9]).
The method described above was implemented as a C++/CUDA library with a Python interface. The CAD model of the room is shown in Fig. 3, and Fig. 4 pictures the early-time pressure field computed for a point source, showing diffraction at some furniture and vertical slats. Computing 2 s-long RIRs at 4 mm resolution for all the receiver positions takes about 50 minutes on an RTX5090 GPU.

Figure 3: CAD model input to the room simulation with speaker S4 highlighted.

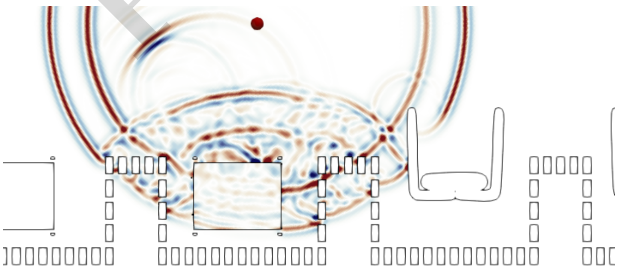

Figure 4: Simulated pressure field generated from 3kHz Ricker pulse at red dot location.

4. Materials

Because precise material information was not available, material admittance functions were defined manually, using absorption tables from the literature as a starting point. Rational positive-real admittance functions were derived from the input absorption values by a non-linear optimization procedure, the details of which fall outside the scope of this study. The material parameters of the largest surfaces were manually adjusted to improve agreement with the measured reverberation times while maintaining physically plausible absorption values for the respective materials. The final material absorption values, computed from the admittances by the Paris formula, are shown in Fig. 5 and Table 1.

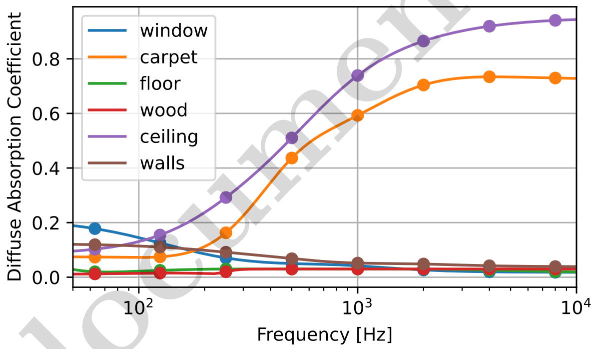

Figure 5: Final diffuse absorption coefficients derived from the calibrated material admittances.

5. Speaker Modeling

Because a directional characterization of speaker S4 was not available, the loudspeaker was represented directly within the FD model by discretizing its geometry and modeling the driver through the boundary-normal velocity source term Q in Eq. (7). To account for cone breakup [13], two excitation modes were used (Fig. 6): the main cone and dust cap at low frequencies, and only the dust cap above a 2 kHz crossover. The driving signal for the combined modes was calibrated against the pressure-difference measurements of the microphone pair in Fig. 2, while the on-device microphone was reserved to validate the simulated off-axis response (see results in Fig. 7).

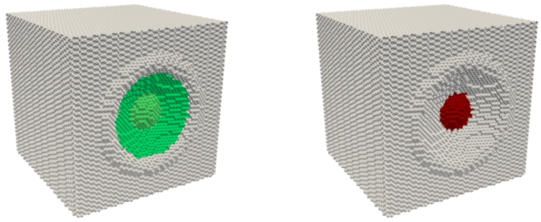

Figure 6: Voxelized speaker model showing driven boundary areas for the pistonic (left) and dust-cap (right) speaker modes.

Table 1: Material diffuse absorption coefficients at octave frequencies.

Elements	63Hz	125Hz	250Hz	500Hz	1kHz	2kHz	4kHz	8kHz
window, blinds	0.178	0.125	0.071	0.050	0.042	0.026	0.020	0.018
carpet, armchairs	0.073	0.075	0.163	0.437	0.593	0.704	0.734	0.730
floor, pillar	0.020	0.025	0.030	0.030	0.030	0.030	0.025	0.020
wood: slats, tables, bench, sideboards, speakers	0.012	0.015	0.020	0.030	0.030	0.030	0.030	0.030
ceiling	0.103	0.154	0.292	0.510	0.739	0.865	0.919	0.941
walls	0.119	0.110	0.092	0.068	0.052	0.048	0.042	0.039

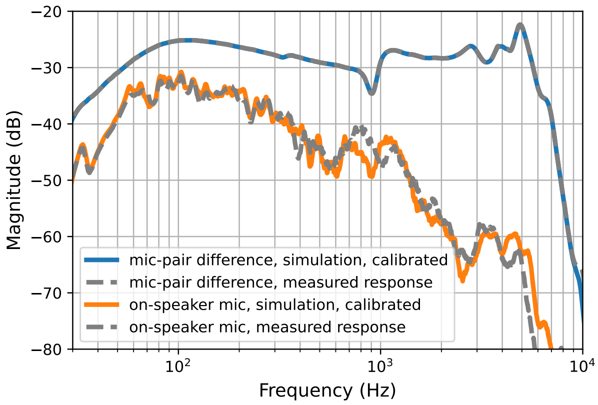

Figure 7: Speaker calibration response (1/8-octave smoothing).

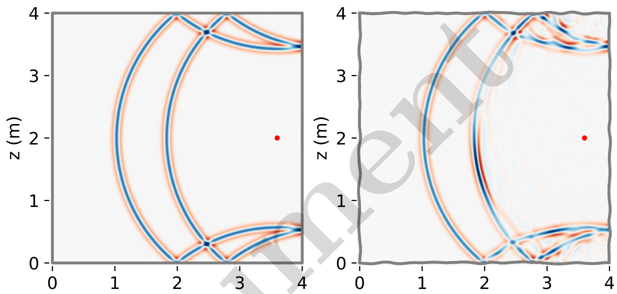

Figure 8: Comparison of waves reflected from a smooth (left) boundary and a boundary with the random displacements (right) added. A point-source 2kHz Ricker excitation is used, located at the red dot.

6. Geometry-based Scattering

Initial simulations showed an unrealistic increase in reverberation time at high frequencies, which was not seen in the measurements. This problem was explained by perfectly specular reflections between two opposite parallel walls, causing flutter echoes.

To address this issue, a small amount of roughness was added to the wall surfaces by displacement along their surface normal according to a 3-D noise function. A stochastic perturbation was used because the unresolved roughness and impedance variations responsible for the observed scattering are not known explicitly. The parameters were varied empirically, with good agreement obtained for a displacement standard deviation of 9 mm and a characteristic length scale of 23 cm. Fig. 8 shows an example of the resultant scattering for a simple $4 \times 4 \times 4$ m cube.

Fig. 9 shows RT30 values averaged over 50 randomly selected receiver positions. The smooth-wall model exhibits the unrealistic high-frequency increase described above, whereas rough walls yield good agreement with the measurements. Both simulations used identical boundary admittances, and the added roughness increased wall surface area by less than 1%.

7. Results and Analysis

Results of the simulation are analyzed in three positions on the receiver grid labeled P1 (3.41m, 5.87m, 1.0m), P2 (0.41m, 0.32m, 1.0m) and P3 (2.81m, 3.77m, 1.45m). The computed RIRs at positions P2 and P3 are plotted in Fig. 10. The agreement between the envelopes of the measured and simulated RIRs suggests that the low-order reflections of the sound field are accurately captured. The simulated FRFs for the same receivers are shown in Fig. 11, where 1/32-octave smoothing has been applied to allow visual comparison at the higher frequencies where modal density is high. A good match is observed for the detailed modal behavior at low frequencies up to a few hundred Hertz as well as for the smoothed envelopes at higher frequencies.

To quantify the agreement between the simulated and measured results, error metrics were computed following the methodology proposed in [10], with the results summarized in Table 2. Metric E_s quantifies the similarity of the FRFs between 30 Hz and 300 Hz, showing an average discrepancy of 19.5%. The mean frequency difference for resonance peaks, E_p, is about 1%, indicating accurate representation of the physical room geometry, at least at long wavelengths. Lastly, the metric E_d relates to discrepancies in the absorption at the room's surfaces. The mean error of 4.3% indicates a close match of the temporal decay, which is corroborated by the match of the position-averaged reverberation time curves shown earlier in Fig. 9.

The dense measurement grid allows for detailed visualization of the spatial sound field, as shown for four frequencies in Fig. 12. The strong agreement at

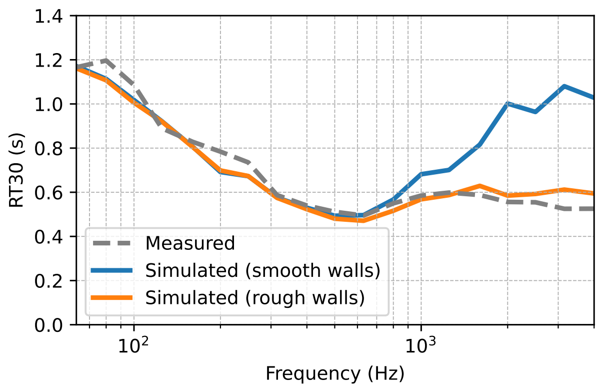

Figure 9: Comparison of simulated and measured reverberation times, averaged over a random selection of 50 receiver-grid locations.

Table 2: Measures of error (in %) between the measured and simulated FRFs at three receiver positions. The frequency range considered is $30 \leq f \leq 300$ Hz.

metric \ position	P1	P2	P3	mean
E_s	22.2	20.7	15.6	19.5
E_p	0.97	1.12	0.99	1.03
E_d	4.38	3.70	4.75	4.28

the two lowest frequencies supports the accuracy of the simulations. At higher frequencies, discrepancies are observed, likely due to imperfections in geometry or materials, though the overall characteristics of the measured fields remain well represented.

8. Conclusion

This study demonstrated practical FD simulation of a measured room containing centimeter-scale geometric detail without manual level-of-detail reduction. Agreement with measurements across multiple metrics supports the use of regular-grid FD methods for realistic room-acoustic simulation. To address high-frequency discrepancies arising from unresolved surface roughness, a geometry-based scattering approach was introduced and shown to mitigate the unrealistic high-frequency reverberation-time increase observed for smooth surfaces.

Some remaining discrepancies, primarily at high frequencies, may be attributed to uncertainties in material parameter estimation or imperfections in the geometric model. Future work will investigate how the proposed scattering model relates to the scattering parameters used in current geometrical-acoustics methods. An extension of the source model to the full audio bandwidth will also be considered.

References

[1] C.-H. Jeong, "Design, simulation, and virtual prototyping of room acoustics," in *Proc. Int. Cong. Acoustics (ICA)*, Gyeongju, Korea, 2022.

[2] C.-H. Jeong, Y. Xia, Y. H. Seo, Ó. H. Pjetursson, E. Arvidsson, and P. Hiselius, "Input data and geometrical details for room acoustic simulations," in *Proc. DAS/DAGA*, 2025.

[3] S. Siltanen, T. Lokki, L. Savioja, and C. Christensen, "Geometry reduction in room acoustics modeling," *Acta Acust united Ac.*, vol. 94, pp. 410–418, 2008.

[4] S. Pelzer and M. Vorlaender, "Frequency- and time-dependent geometry for real-time auralizations," in *Proc. Int. Cong. Acoustics (ICA)*, vol. 5, Sydney, Australia, 2010.

[5] V. Martin, I. Engel, and L. Picinali, "Effects of geometrical acoustics model simplification on binaural reverberation," eng, *IEEE/ACM Trans. Audio Speech Lang. Process.*, vol. 33, pp. 3480–3493, 2025.

[6] L. Friede, C. Tuna, F. Knauff, A. Prinn, K. Ersinadim, and A. Walther, "Multi-purpose room impulse response dataset measured on a 3D spatial grid," in *AES 156th Convention*, Madrid, Spain, 2024.

[7] S. Shelley and D. Murphy, "The modeling of diffuse boundaries in the 2-d digital waveguide mesh," *IEEE/ACM Trans. Audio Speech Lang. Process.*, vol. 16, pp. 651–665, 2008.

[8] K. Kowalczyk, M. Van Walstijn, and D. Murphy, "A phase grating approach to modeling surface diffusion in FDTD room acoustics simulations," *IEEE/ACM Trans. Audio Speech Lang. Process.*, vol. 19, pp. 528–537, 2011.

[9] B. Hamilton and S. Bilbao, "On finite difference schemes for the 3-D wave equation using non-Cartesian grids," in *Proc. Sound and Music Computing Conf. (SMC)*, Stockholm, Sweden, 2013, pp. 592–599.

[10] A. Prinn, Z. Xu, and E. Habets, "Measures of validation for computational room acoustics," in *Proc. 11th Forum Acusticum*, Málaga, Spain, 2025.

[11] J. W. Smits and S. Bilbao, "Optimised implicit finite-difference schemes for the wave equation with admittance boundary conditions," *J. Acoust. Soc. Am.*, vol. 157, pp. 2168–2179, 2025.

[12] J. Meyer, T. Lokki, and J. Ahrens, "Perceptual detection thresholds for numerical dispersion in binaural auralizations of two acoustically different rooms," *J. Acoust. Soc. Am.*, vol. 152, pp. 2266–2276, 2022.

[13] W. Klippel and J. Schlechter, "Measurement and visualization of loudspeaker cone vibration," in *AES, 121st Conv.*, San Francisco, USA, 2006.

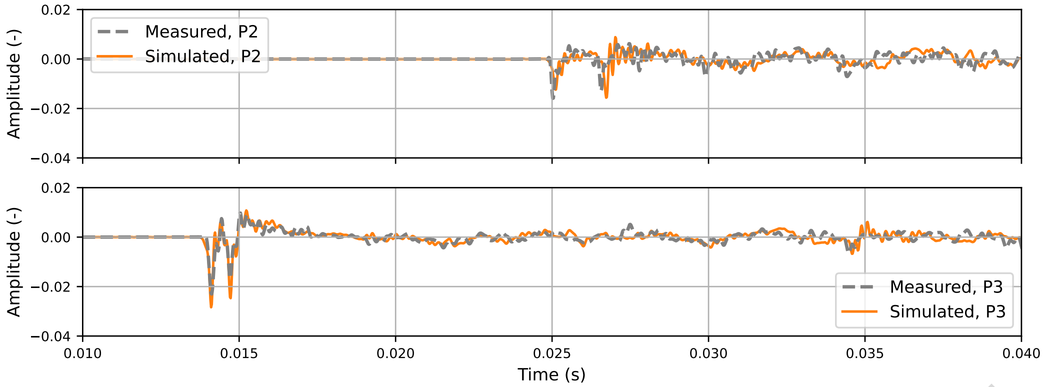

Figure 10: Early-time impulse response comparison between simulation and measurement.

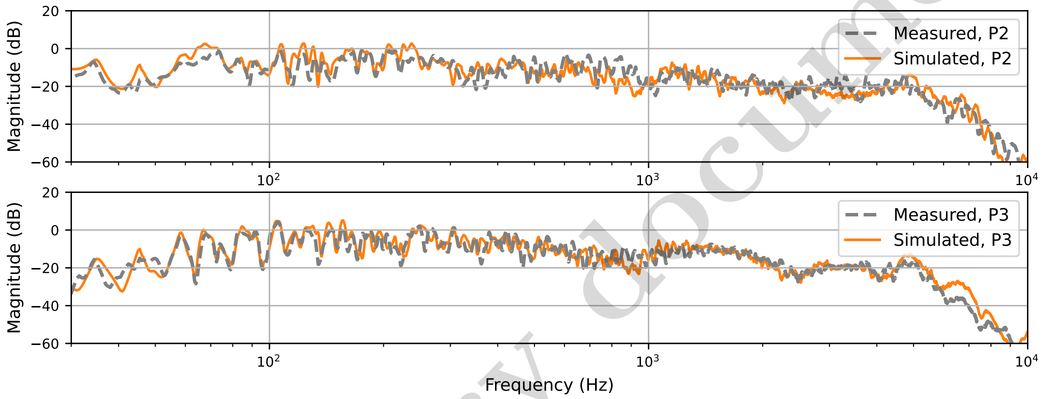

Figure 11: Frequency response comparison between simulation and measurement.

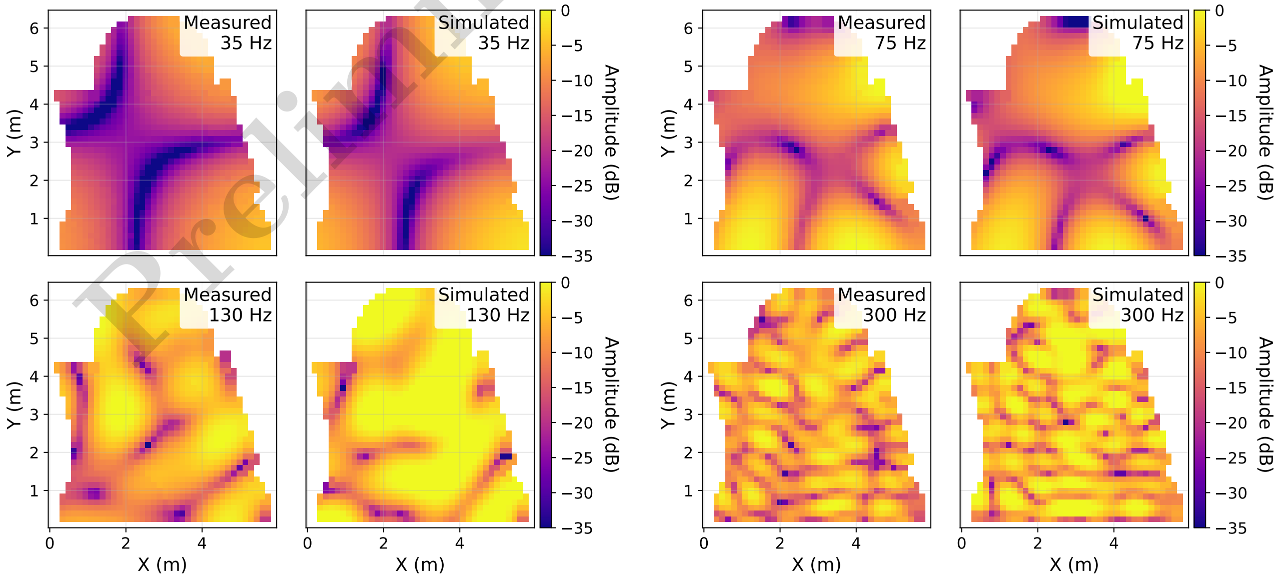

Figure 12: Pressure field distribution comparison of measurement and simulation.